

Magnetic Flux Tubes Illuminated by Pulsar Winds

YIFAN SUN ^{1,2} C.-Y. NG ^{1,2} AND SIMING LIU ³

¹*Department of Physics, The University of Hong Kong, Pokfulam Road, Hong Kong*

²*Hong Kong Institute for Astronomy and Astrophysics, The University of Hong Kong, Pokfulam Road, Hong Kong*

³*School of Physical Science and Technology, Southwest Jiaotong University, Chengdu, 610031, People's Republic of China*

ABSTRACT

Observations of linear structure connecting pulsars to gamma-ray halos reveal injection of TeV electrons into the interstellar medium (ISM). In some cases, this could be attributed to nearly scattering-free electron transport along large-scale magnetic fields connected to pulsar winds with very slow diffusion across the field lines. In this work we model this process with a magnetic flux tube emerging from the pulsar and attached to the ISM magnetic field. We show that particles in this case have an anisotropic distribution of magnetic pitch angle, such that the overall emission is highly beamed. We apply this model to pulsar tails and filaments, including the extended X-ray and TeV emission associated with PSR J1740+1000 and the misaligned X-ray jet in the Guitar Nebula, to constrain their particle population and magnetic fields.

Keywords: Pulsars (1306), Pulsar wind nebulae (2215), Gamma-rays (637), Interstellar medium (847), Radio interferometry (1346)

1. INTRODUCTION

Evolved pulsar wind nebulae (PWNe) that have left the parent supernova remnant often show bow-shock structure and a long tail, since they travel supersonically through the interstellar medium (ISM). These tails trace the pulsar motion over tens of parsecs and consist of synchrotron-emitting particles that can be observed in radio and/or X-ray. Recent numerical simulations suggest that the magnetic field should align with the tail, as it is formed by the swept-up ISM magnetic fields left behind (B. Olmi & N. Bucciantini 2019a). A few bow-shock PWNe are also found to be associated with diffuse gamma-ray emission along the tail direction (e.g., H. E. S. S. Collaboration et al. 2011; Z. Cao et al. 2025). Spectral fitting suggests that the pulsar is able to provide enough high-energy particles to produce the observed gamma-ray emission via inverse Compton (IC) scattering. This however requires the particles to keep most of their energy during transport through the tail. To explain the multiwavelength morphology of these TeV sources, there have been previous attempts to consider complicated magnetic field geometry with a significantly aligned component to transport the par-

ticles from the PWN to TeV-emitting regions (e.g., Y. Bao et al. 2025; K. Yan et al. 2025).

Another related structure is misaligned X-ray filaments in bow-shock PWNe. (see J. T. Dinsmore & R. W. Romani 2024). They are highly collimated, much narrower than pulsar tails, and extend to a few parsecs. More intriguingly, they often show large misalignment angle with the pulsar proper motion direction, and some even point ahead of the pulsar. They are only detected in X-rays with no radio counterparts, and their spectra are well described by a single power law without cooling. Such linear structure is suggested to be due to high-energy particles injected into pre-existing magnetic field lines in the ISM when the PWN passes by (R. Bandiera 2008; B. Olmi & N. Bucciantini 2019b; B. Olmi et al. 2024). Previous studies modeled these with aligned magnetic fields (e.g., the “magnetic bottles/antibottles”; M. V. Barkov et al. 2019b) with a coherence length much larger than the physical length size of the filaments, as indicated by the minimal cooling observed.

In this paper, we model these linear structures using magnetic flux tubes. We consider a one-zone leptonic model, where the same populations of electrons produce both the synchrotron (radio to X-ray) and IC (gamma-ray) emission. The magnetic field is assumed to be well aligned and the particles are bound to the field lines, following a near ballistic trajectory. We demonstrate

that this setup can produce an electron population with anisotropic pitch angle distribution, and the emissions are beamed along the magnetic field lines. This modifies the synchrotron emissivity and creates unique observational signatures. One important consequence is that part of the flux tube could be unobservable due to the beaming and the view angle. This can result in a hard cutoff in the observed image. There have been studies of anisotropic leptonic emission in the context of other astrophysical sources, e.g., in pulsar emission (R. I. Epstein 1973; R. I. Epstein & V. Petrosian 1973), blazars, and gamma-ray bursts (Y.-P. Yang & B. Zhang 2018). These sources are more beamed such that the anisotropy is more apparent. In previous works on PWNe, however, this anisotropy is in general not considered, and the electrons are often assumed to be isotropic. The model by itself is extremely versatile. In addition to the above-mentioned two types of sources, it can in principle be applied to any source where the magnetic field lines are sufficiently aligned, i.e., when the physical length scale is much smaller than that of the magnetic field turbulence.

In Section 2, we discuss the basic setup and observational signatures of the magnetic flux tube model. We apply the model to two different type of sources: in Section 3, we study the PWN tail of PSR J1740+1000 which is found to be associated with an offset TeV gamma-ray source, and in Section 4, we study the misaligned filament formed by outflow from bow-shock PWNe, with Guitar Nebula as an example.

2. MAGNETIC FLUX TUBE MODEL

2.1. Assumptions and setup

The geometry of the magnetic flux tube is shown in Figure 1. High-energy particles are injected from the pulsar end of the tube, where the magnetic field strength is larger than the exiting end. The latter is assumed to have a typical ISM field strength of a few μG . The B -field inside the tube is taken to be nearly unidirectional, with slight divergence due to the decreasing field strength and conservation of magnetic flux. In the figure we illustrate the case that the field strength scales as the distance z from the pulsar. $B \propto z^{-2}$. This gives a flux tube with straight edges, but we note that this dependence can be arbitrary in general. The particles inside the tube are bounded to the magnetic field lines without any scattering. This means that the energetic relativistic particles effectively move across the tube at nearly speed of light. The physical size of a magnetic flux tube is limited by the ISM turbulence length scale, which is suggested to be up to several hundred parsecs (M. C. Beck et al. 2016). The particle traversal time is then ~ 1 kyr, significantly shorter

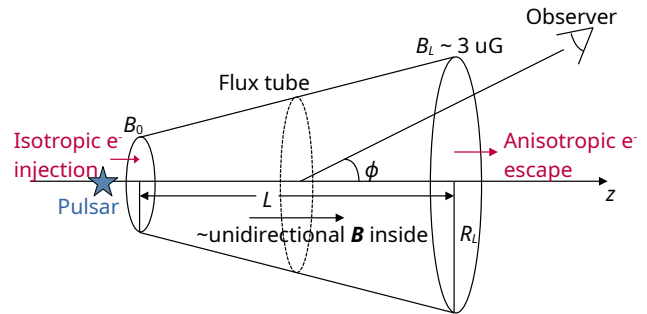


Figure 1. Illustration of magnetic flux tube model. High-energy electrons accelerated in the PWN are injected into the magnetic flux tube and transport to the right. The magnetic field is assumed to be pointing to $+z$ -direction and $B \propto z^{-2}$ for this figure. The flux tube has length L and radius R_L at the exit end. ϕ is the global viewing angle defined using the axis.

than the typical synchrotron cooling times of $\tau_{\text{syn}} = 13.0(E_e/40 \text{ TeV})^{-1}(B/5 \mu\text{G})^{-2} \text{ kyr}$. We therefore ignore any radiative energy loss in the flux tube and consider a time-independent steady-state solution. The viewing angle ϕ between the line of sight and the symmetry axis will significantly alter the observed source morphology and other physical parameters.

2.2. Particle evolution

The evolution of particle pitch angle distribution in a magnetic field is described by a simplified Vlasov equation (G. Qin et al. 2006):

$$\mu v \frac{\partial f}{\partial z} + \frac{d\mu}{dt} \frac{\partial f}{\partial \mu} = 0, \quad (1)$$

where $f(z, \mu)$ is the distribution function of particles and $\mu = \cos \alpha$ is the cosine of the local magnetic pitch angle α .

The term $d\mu/dt$ describes the pitch angle evolution. For a slowly varying magnetic field, it can be shown that the magnetic moment of a particle, which is proportional to v_{\perp}^2/B , is conserved (M. S. Longair 2011). Taking the time derivative gives the following expression due to the so-called magnetic mirroring effect,

$$\frac{d\mu}{dt} = -\frac{1 - \mu^2}{2B} \frac{\partial B}{\partial z}. \quad (2)$$

Note that the spatial variation of the magnetic field $B(z)$ will be chosen later depending on the source geometry. The above two equations can be combined to form a single partial differential equation, which can be solved to obtain

$$f(z, \mu) = f_0 \left(\sqrt{1 + \frac{\mu^2 - 1}{a}} \right) \quad (3)$$

using the initial condition $f(0, \mu) = f_0(\mu)$ at the boundary $z = 0$, where $a \equiv B(z)/B(0)$. This suggests that the particle distribution can also be viewed as a function of the magnetic field strength. In the following discussion, we assume B is a decreasing function of z and hence $a < 1$.

One particularly simple but physically interesting model is isotropic particle injection at $z = 0$. In this case, $f(0, \mu)$ is a constant independent of μ . Since $\mu \in [\sqrt{1-a}, 1]$ in Equation 3, the pitch angle distribution function $f(z, \mu)$ will be constrained within a cone of $\sin \alpha \leq \sqrt{a}$. This cutoff value is a function of the magnetic field strength and hence depends on the physical distance traveled. There will be no particles with pitch angle larger than this cutoff value. Inside this cone, the number of particles with pitch angle $[\alpha, \alpha + d\alpha]$ remains constant. This shows that, in this simple model of a flux tube with a decreasing magnetic field, the particles tend to form a beam along the magnetic field line with a decreasing cutoff of the pitch angle.

2.3. Emission from anisotropic electron population

The anisotropic pitch angle distribution of electrons inside the magnetic flux tube can change the emissivity of both the synchrotron and IC emission from the standard leptonic model. For the former, the radiation power per unit solid angle $d\Omega$ per unit frequency $d\omega$ for a single electron of energy $\gamma m_e c^2$ and pitch angle α is given by (e.g., G. B. Rybicki & A. P. Lightman 1979; Y.-P. Yang & B. Zhang 2018),

$$\frac{dW}{d\omega d\Omega} = \frac{\omega_B}{2\pi \sin^2 \alpha} \frac{e^2}{3\pi^2 c} \left(\frac{\omega\rho}{c}\right)^2 \left(\frac{1}{\gamma^2} + \theta^2\right)^2 \left[K_{2/3}^2(\xi) + \frac{\theta^2}{(1/\gamma^2) + \theta^2} K_{1/3}^2(\xi) \right]. \quad (4)$$

In this equation, ω_B is the gyro frequency, ρ is the radius of curvature of the electron, θ is the angle between line of sight and the electron's velocity vector, and $K_\nu(\xi)$ is the modified Bessel function with the argument $\xi = (\omega\rho/3c)(1/\gamma^2 + \theta^2)^{3/2}$. As mentioned, the electron population will have a pitch angle distribution of $\sin \alpha \leq \sqrt{a}$. If we assume an exponential cutoff powerlaw distribution of electrons for PWNe, with $dN/dE \propto E^{-1} \exp(-E/110 \text{ TeV})$, Equation 4 can be integrated over the electron's pitch angle α and energy γ to obtain the emission coefficient.

Figure 2 shows the results for $\phi = 0.1$ and $B_0 = 100 \mu\text{G}$. We also plot the emission from an electron population where such effect is ignored. The two are normalized such that the number of particles inside the cone $\sin \alpha \leq \sqrt{a}$ are the same. The plot shows a hard cutoff in the observed emission when $\sin \phi < \sqrt{a}$, i.e., all elec-

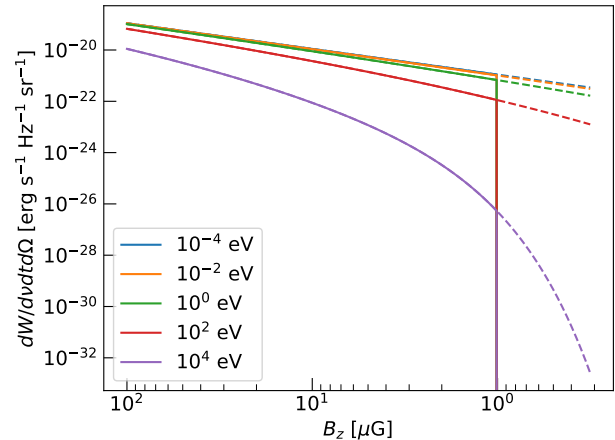


Figure 2. Synchrotron spectral intensity, i.e., energy per unit time per steradian per frequency, for a group of particles evolving along the magnetic flux tube at different photon energies. This assumes a view angle of $\phi = 0.1$ and the magnetic field strength of $B_0 = 100 \mu\text{G}$ at the injection end. The electron distribution is taken as an exponential cutoff power law $dN/dE \propto E^{-1} \exp(-E/110 \text{ TeV})$. The solid lines show the emission from the predicted evolution of an isotropic electron population injection. The dashed line shows the emission from the same population of electrons but without pitch angle evolution, consistent with standard semianalytical formula. They agree until some cutoff point, where the pitch angle of all particles becomes smaller than the view angle ϕ , indicating a finite viewable length of the magnetic flux tube.

trons evolve to have pitch angles smaller than the view angle. This is due to beaming of the synchrotron emission, such that the emission is confined within a cone of $\sim 1/\gamma$ along the particle velocity direction, where γ is the particle's Lorentz factor. Because of the cutoff, the physical length of the magnetic flux tube can be longer than what is observed. We also note that if the flux tube is pointing away from us, i.e., $\phi > \pi/2$, all the emission will not be observable unless some other effects, such as scattering, that randomize the pitch angle distribution.

For the IC process with cosmic microwave background photons, while it is independent of the magnetic field and the pitch angle, the emission is still expected to be beamed along the particle velocity direction due to anisotropic particle momentum distribution. This modifies the IC emission profile (e.g., A. C. M. Lai & K. C. Y. Ng 2023). Trying to solve this numerically for arbitrary electron and seed photon distributions proved to be computationally infeasible for our application, due to the number of parameters that needed to be integrated over. We note that the upscattered photons from these electrons are beamed within an angle of $\sim 1/\gamma$, given by the Lorentz transformation between the electron rest

frame and the observer frame (G. B. Rybicki & A. P. Lightman 1979). This allows us to approximate the IC emission to be along the electron’s velocity vector, and the directional dependent emission profile is directly proportional to the number of particles moving along the line of sight. There will be a similar cutoff as in the synchrotron process.

2.4. Observational signatures

To compare with observations, we adopt $B \propto z^{-2}$ which gives a truncated cone shape flux tube as shown in Fig. 1. We divide the tube into small discrete volumes and calculate the particle pitch angle distribution. The synchrotron emission in each cell is computed using the `naima` package (F. A. Aharonian et al. 2010; V. Zabalza 2015) and then all cells are summed over the line of sight to obtain a sky image. Figure 3 shows the resulting images with different viewing angles. It is clear that the X-ray emission always peaks near the injection end, while the IC emission peaks near the exit end. The former is due to the stronger magnetic field strength, and the latter can be attributed to combination of projection effect and the decreasing pitch angle of the particles, as discussed in Section 2.2.

In the following discussion, we take the cutoff point as the exit end of the flux tube, since the rest is not observable. The viewing angle ϕ is an important parameter in the model that sets the B -field ratio between the injection and exit ends as $B_0 = B_L / \sin^2 \phi$. For typical ISM field strength at the exit end, e.g., $3 \mu\text{G}$ in the case of Figure 3, this requires $B \sim 10\text{--}100 \mu\text{G}$ at the injection end for moderate ϕ . Due to conservation of magnetic flux, the equation above also determines the radius ratio between the two ends, R_0/R_L , and hence the emission morphology. A small ϕ gives $R_0/R_L \ll 1$, resulting in a short, cone-like X-ray tail with large opening angle (see Figures 3a and b). On the other hand, if viewed edge-on, i.e., large ϕ , the X-ray emission would have constant width with a more gradual decrease in the surface brightness (see Figures 3e and 3f).

As argued above, the effect of radiative cooling should be minimal during the short traversal time of the particles in the flux tube. We therefore do not expect significant variation of the emission spectrum. However, the reducing B -field would shift the high-energy cutoff to lower energies. Such effect could be observable with spatially resolved spectrum obtained from deep X-ray observations. Moreover, the ordered magnetic field in the flux tube would produce synchrotron emission with linear polarization fraction close to the maximum allowed value (see P. C. W. Lai et al. 2025, for details).

Finally, we note that in the simulated images we did not consider the effect of finite gyroradius for the synchrotron-emitting particles. Accounting for this will smooth out the edge of the flux tube in the image. For electrons emitting photons of energy E_{keV} , the gyroradius has an angular scale of

$$\theta = 26'' E_{\text{keV}}^{1/2} B_{\mu\text{G}}^{-3/2} d_{\text{kpc}}^{-1} \quad (5)$$

(M. de Vries et al. 2022). This is a few arcseconds for $B \sim 10 \mu\text{G}$ and $d \sim 1 \text{ kpc}$, comparable with the resolution limit of X-ray telescopes such as the Chandra X-ray Observatory (CXO). In the sources that we will discuss in the following sections, such smoothing effect can be safely ignored.

3. APPLICATION 1: PSR J1740+1000 TAIL

3.1. Multiwavelength observations of J1740

PSR J1740+1000 (hereafter J1704) is a middle-aged pulsar with characteristic age $\tau_c = 114 \text{ kyr}$, spin-down luminosity $\dot{E} = 2.3 \times 10^{35} \text{ erg s}^{-1}$ and dispersion measure-inferred distance of 1.2 kpc (W. Benbow et al. 2021; M. Rigoselli et al. 2022, and references therein). It has been observed in X-rays with CXO and XMM-Newton. As shown in Figure 4, the XMM image reveals a $5.5'$ long tail trailing the pulsar (O. Kargaltsev et al. 2008). The high Galactic latitude ($b = 20.268^\circ$) of J1740 indicates that it is likely moving at a high speed out of the Galactic plane, which can be confirmed with future proper motion measurement. The extended X-ray emission is therefore suggested to be a bow-shock PWN (W. Benbow et al. 2021). The tail shows a nearly conical shape at the tip with a width of $\sim 1.5'$, then beyond $3'$ from the pulsar the width stays mostly constant, and the orientation slightly bends to the west. The XMM data found a power-law spectrum with $\Gamma = 1.75 \pm 0.03$ for the overall $5.5'$ tail (W. Benbow et al. 2021). Recently, a reanalysis of the same XMM data shows no significant spectral variation along the tail (G. Brunelli et al. 2025), suggesting minimal cooling for the particles. The CXO observation of the tail, on the other hand, suggests a harder spectrum with $\Gamma = 1.2 \pm 0.2$ in a shorter length of $2.6'$ (J. T. Dinsmore & R. W. Romani 2024). In addition, we analyze radio observation of the tail taken with the Karl G. Jansky Very Large Array (VLA) at the 10 cm band. The detailed analysis and results are described in the Appendix A, and the total intensity map is shown in Figure 4. No radio emission is found from the tail and we obtained a 3σ upper limit of 3.5 mJy .

Recently, TeV gamma rays are detected with LHAASO near J1740. The emission peaks at $12'$ from the pulsar along the X-ray tail direction and is slightly

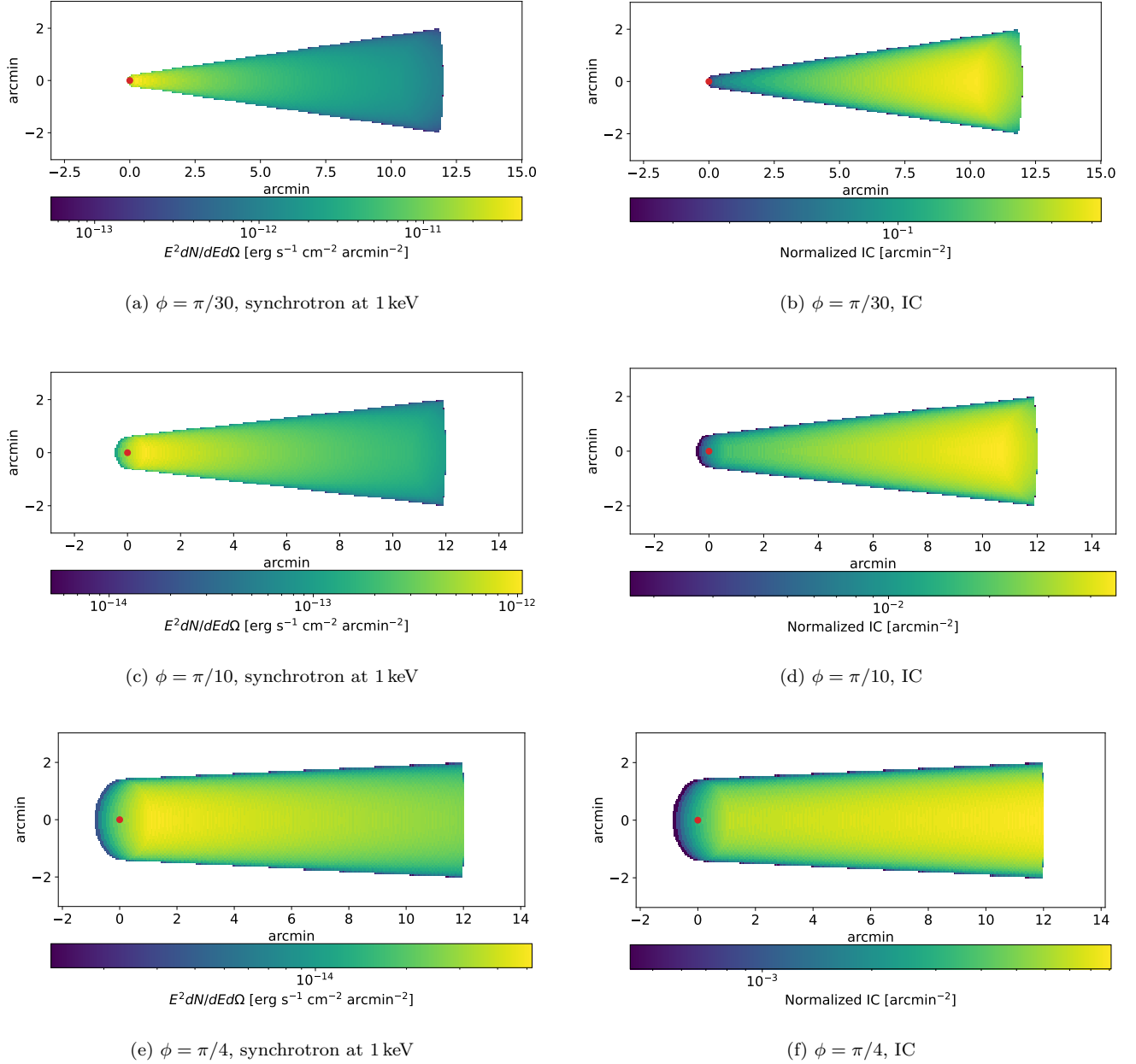


Figure 3. Simulated synchrotron X-ray images at 1 keV (left column) and IC gamma-ray images (right column) for the magnetic flux tube viewed at different ϕ . The red dots indicate the center of the injection end. We assume $R_L = 2'$, $B_L = 3 \mu\text{G}$, and an electron distribution of $dN/dE \propto E^{-1} \exp(-E/110 \text{ TeV})$. The projected length is fixed at $12'$ by changing the physical length of the flux tube with $L = 12'/\sin \phi$. The magnetic field at the injection end is set by $B_0 = B_L/\sin^2 \phi$.

extended with angular scale $\lesssim 0.147^\circ$ (Z. Cao et al. 2025). The spatial distribution of the TeV emission can be described using a diffusion-dominated model. The corresponding diffusion coefficient for energy $E > 25 \text{ TeV}$ is $D = 3.55 \times 10^{26} \text{ cm}^2 \text{ s}^{-1}$. A phenomenological fitting of TeV spectrum using a simple one-zone leptonic model gives an electron distribution of $dN/dE \propto E^{-p} \exp(-E/E_{\text{cut}})$, with the index $p = 2$ and a cutoff energy of $E_{\text{cut}} = 110 \text{ TeV}$. The nondetection of

X-ray counterpart implies a low magnetic field strength $\lesssim 1.4 \mu\text{G}$ at the TeV center (G. Brunelli et al. 2025).

3.2. Model setup with an additional diffusion zone

Assuming that the observed X-ray and gamma-ray emission trailing J1740 is powered by the same population of particles injected by the PWN, we employ the magnetic flux tube model to explain the offset between the two emissions. Our model considers only the bal-

listic transport of highest energy particles but ignores advection of particles strongly coupled with the background plasma as suggested by magnetohydrodynamics (MHD) simulations of bow-shock PWNe (e.g., [M. V. Barkov et al. 2019a](#)). While advection could be the dominant effect for low-energy electrons, we argue that it cannot solely explain the transport of the > 10 TeV electrons that are responsible for the offset gamma-ray emission. This initial postshock flow speed can be very high ($\approx c$) near the pulsar, but it decelerates downstream to nearly the pulsar speed (several hundreds km s^{-1}) as both numerical simulations and observations show ([C.-Y. Ng et al. 2010](#); [G. Morlino et al. 2015](#)). As a result, the traversal timescale over the parsec-long tail would be much longer than the cooling timescale of the > 10 TeV electrons, hence requiring an alternative mechanism such as the flux tube model.

The critical electron energy at which the dominant transport mechanism transitions from advection to ballistic can be estimated from the gyroradius of the electrons. For 1 keV synchrotron X-rays, they correspond to 30 TeV electrons assuming a magnetic field of $20 \mu\text{G}$, and the electron gyroradius would be 0.002 pc. This is smaller than the observed ~ 0.1 pc radius of the X-ray tail so that these electrons are confined in the tail. MHD simulations have shown that a turbulent magnetic field can develop at scales of a few percent of the tail radius ([B. Olmi & N. Bucciantini 2019c](#)), corresponding to a few times 0.001 pc. This is comparable with the gyroradius of these X-ray-emitting electrons, implying that they are not bound to these small-scale field lines and instead follow a ballistic transport along the large-scale magnetic field in the tail.

That being said, it is challenging to explain the gamma-ray observation with a simple flux tube model. This is because, in our model, the particles continuously leave the system and then become unobservable with a very low radiation efficiency in the flux tube, thus requiring a large injection power from the pulsar. A simple leptonic fit to the TeV emission yields a total electron energy of 2.6×10^{45} erg for an exponential cutoff power-law distribution ([Z. Cao et al. 2025](#)). Comparing this with the particles' transversal time of $\sim 10^9$ s across a 10 pc long tube suggests that a power input of $\sim 10^{36} \text{ erg s}^{-1}$ is needed, significantly larger than the spin-down luminosity of $2.3 \times 10^{35} \text{ erg s}^{-1}$ for J1740.

The above estimate hints at additional emission from particles after they left the flux tube. We model this as an additional diffusion zone. This is also physically motivated: as the B -field inside the tube decreases to a strength comparable to the ISM field, the two fields could mix such that particles are scattered between field

lines. This scattering randomizes the pitch angle distribution, which makes the emission visible again. Emission energy loss is significant when diffusion dominates as it increases time for particles to travel through the region.

To model this, we follow the treatment by [A. M. Atoyan et al. \(1995\)](#) to derive the particle evolution in a spherically symmetric diffusion zone. For a time independent exponential cutoff power law distribution of injected particles, i.e. $dN/d\gamma dt = Q_0 \gamma^{-p} \exp(-\gamma/\gamma_{\text{cutoff}})$, where Q_0 is the normalization factor to be determined by matching the observed flux and γ the Lorentz factor of the electrons with a high energy cutoff at γ_{cutoff} , the resulting distribution function of electrons as a function of radius r and age t is

$$f(r, t, \gamma) = \frac{Q_0 \gamma^{-p} e^{-\gamma/\gamma_{\text{cutoff}}}}{4\pi D(\gamma)r} \text{erfc} \left(\frac{r}{2\sqrt{D(\gamma)t_\gamma}} \right). \quad (6)$$

Here $t_\gamma = \min(t, 0.75/(p_2\gamma))$ is an empirical estimate of whether the transport of particles at given energy γ is limited by the age or the cooling timescale. We assume a quadratic cooling relation of $dE/dt = p_2\gamma^2$ with the constant p_2 that accounts for both IC and synchrotron processes. The diffusion coefficient is assumed to follow a power-law dependence of $D = D_{100}(E/100 \text{ TeV})^\delta$, with $\delta = 1/3$ from the Kolmogorov turbulence model ([A. Kolmogorov 1941](#); [A. U. Abeysekera et al. 2017](#)). We take $D_{100} = 3.55 \times 10^{26} \text{ cm}^2 \text{ s}^{-1}$ based on the LHAASO measurements ([Z. Cao et al. 2025](#)). Finally, the emission from the diffusion zone is computed by integrating the synchrotron and IC emission along the line of sight.

Note that we assume point injection and ignore the transition process from anisotropic to isotropic pitch angle distributions when the particles enter the diffusion zone (see [M. R. Krumholz et al. 2024](#)). We argue that this has no effect on the X-ray emission morphology that we are interested in, since the emission is mostly near the head of the magnetic flux tube. Depending on the model parameters and observing energy band, the relative contribution between the magnetic flux tube and the diffusion zone can vary significantly. A small ϕ enhances the geometric boosting effect in the flux tube so that the diffusion zone contribution is reduced. This also increases the magnetic field near the PWN, therefore further enhancing the tail feature in X-ray. The extended X-ray emission from the diffusion zone can be easily hidden by the background, and the gamma-ray morphology will also deviate from the standard Gaussian-like due to the contribution from the flux tube component. In the limiting case of nearly face-on geometry, $\phi \approx 0$, our model would produce a gamma-ray point source surrounded by faint diffused emission. This could explain some re-

cently identified TeV halos that show two-component structure with strongly suppressed diffusion coefficient (A. U. Abeysekara et al. 2017; S. Recchia et al. 2021).

3.3. Modeling the X-ray and gamma-ray structure

In the modeling, we took $\phi = 0.3$ rad to match the opening angle of the J1740 tail. The length of the flux tube is set to $L = 12'/\sin\phi$ such that its projected length gives the $12'$ offset between the pulsar and the gamma-ray center. We chose R_L to match the observed $1.5'$ width of the injection. The simulated X-ray and gamma-ray images are shown in Figure 5. Our model has successfully captured the characteristics of the X-ray tail of J1740, i.e., the opening angle near the pulsar and the bright emission in the first $\sim 6'$. Beyond that, the simulation predicts fainter emission extending all the way until the end of the $12'$ tail with minor flux enhancement near the center of the diffusion zone. The existing XMM data as shown in Figure 4 lack sensitivity to verify this. Future observations with Einstein Probe Follow-up X-ray Telescope or eROSITA will be useful. For gamma-ray emission, our model shows that it peaks near the diffusion zone, which well agrees with the observation. We note that in principle the flux tube can extend significantly beyond the cutoff point. In this case, we expect two disjoint gamma-ray emission components, one near the cutoff and one at the diffusion zone. These are however difficult to observe given the poor angular resolution of gamma-ray observations in general. If a clear gap is found, it would imply a different B -field strength at the diffusion zone than at the cutoff point of the flux tube.

3.4. Modeling the broadband spectrum

In addition to the emission structure, we also simulate the broadband spectrum of J1740 based on the flux-tube-plus-diffusion-zone model above. We adopt the exponential cutoff particle distribution with $E_{\text{cut}} = 110$ TeV obtained with LHAASO (Z. Cao et al. 2025), and we also follow the same work to consider IC with cosmic microwave background, near infrared (0.25 eV cm^{-3} at 30 K), and far infrared (0.5 eV cm^{-3} at 5000 K) photons. The overall normalization is set by the gamma-ray flux. This gives an injection rate of 3.23×10^{33} erg s $^{-1}$, around 1.4% of the spin-down rate of pulsar J1740. Once the normalization is fixed, the B -field strength is determined by the matching the X-ray flux. We consider only the region of $1.5' \times 6'$ near the pulsar since the XMM measurement covers only a small field of view (see Figure 4). This suggests $B_L = 1.2$ μG at the exit end, corresponding to $B_0 = 14$ μG at the injection end. The former is consistent with the ISM field

strength at this high Galactic latitude (R. Jansson & G. R. Farrar 2012) and is also compatible with the upper limit derived from the nondetection of diffuse X-rays by XMM at the gamma-ray source location (G. Brunelli et al. 2025). Figure 6 shows the simulated broadband spectrum from X-rays to gamma rays and a comparison with the data. We note that our model gives a slightly harder X-ray spectrum ($\Gamma = 1$) than the one observed by XMM ($\Gamma = 1.7$), but closer to the Chandra measurement ($\Gamma = 1.2$; J. T. Dinsmore & R. W. Romani 2024). The softer spectrum can be explained if there is additional emission component by particles not captured by the flux tube. We also tried fitting with a softer injection spectrum and found that $p = 2.5$ well fits the X-ray spectrum but not the gamma-ray one. Finally in Figure 6 we plot the spatial variation of the synchrotron X-ray spectrum along the flux tube. The spectral peak shifts to lower energy while moving away from the pulsar. This is due to the decreasing magnetic field and can be confirmed with spatially resolved spectroscopy from deep X-ray observations in the future.

4. APPLICATION 2: MISALIGNED PWN OUTFLOW

Misaligned PWN outflows are found in several bow-shock PWNe in X-rays. They are resulting from the injection of high-energy particles into well-ordered magnetic filaments in the ISM. Our magnetic flux model therefore would be applicable here. We focus on the most studied PWN filaments — those in the Guitar Nebula powered by the old pulsar B2224+65 with characteristic age $\tau_c = 1120$ kyr and spin-down luminosity of $\dot{E} = 1.2 \times 10^{33}$ erg s $^{-1}$. The pulsar has distance of 0.83 kpc and proper motion of $\mu = 194.1 \pm 0.2$ mas yr $^{-1}$ measured with parallax (A. T. Deller et al. 2019) Chandra X-ray observations show a $2.5'$ long filament extending from the pulsar with a large (110°) misalignment angle from the proper motion direction (M. de Vries et al. 2022; J. T. Dinsmore & R. W. Romani 2024). Its X-ray spectrum is well described by a power law with $\Gamma = 1.6 \pm 1$ and an unabsorbed flux of 6.35×10^{-14} erg s $^{-1}$ cm $^{-2}$ in 0.5–7 keV (J. T. Dinsmore & R. W. Romani 2024). Detailed spatially resolved spectroscopy shows no spectral softening along the filament except near the very end (M. de Vries et al. 2022), which is consistent with our flux tube model prediction. The magnetic field inferred from equipartition is ~ 13 μG near the pulsar and 8 μG further away. A short counterfilament is also observed, which extends at least $20''$ from the pulsar in a direction opposite to the main filament.

In our modeling, we adopt a power-law particle distribution with index $p = 2.2$ inferred from the X-ray

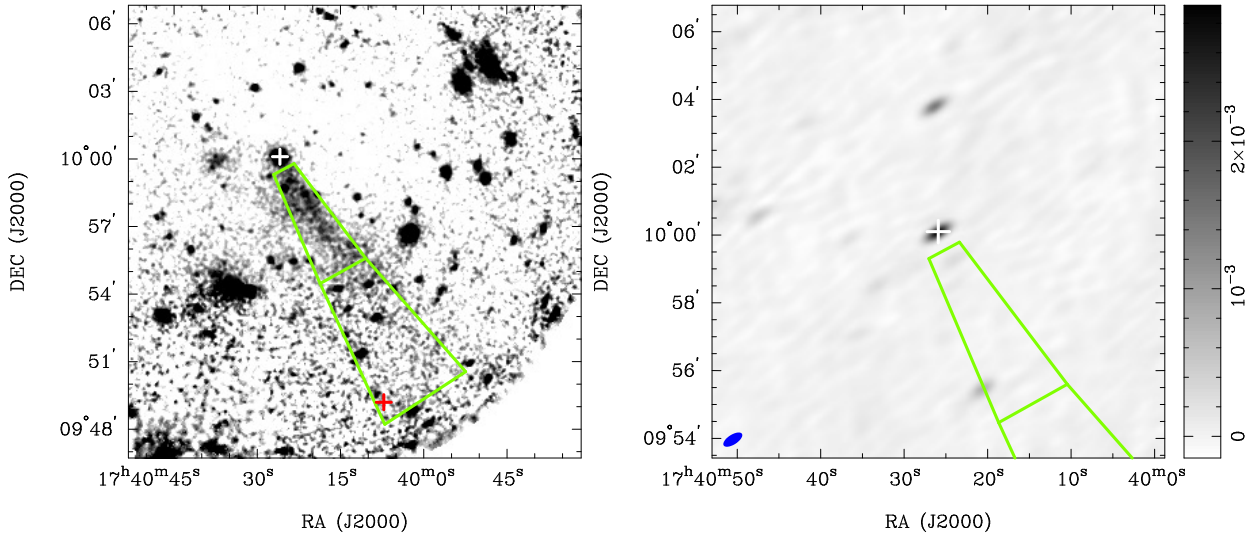


Figure 4. Left: merged and exposure-corrected XMM-Newton image of J1740 tail from MOS 1 and MOS 2 in 0.4–7.2 keV range (ObsIDs: 0803080201, 0803080301, 0803080401, and 0803080501). The white cross marks the position of J1740 and the red cross indicates the center of the TeV source 1LHAASO J1740+0948u. The green region shows the tail as detected by XMM and the full extension assumed in our modeling. Right: VLA total intensity radio map of J1740 at 10 cm. The beam size is shown in lower left. The tail is not detected in the data.

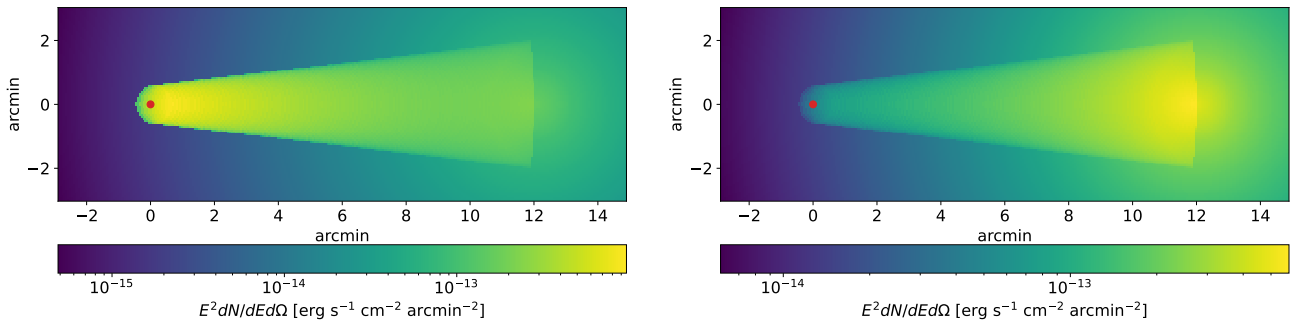


Figure 5. Synchrotron X-ray image at 1 keV (left) and IC gamma-ray image 10 TeV (right), generated using the best-fit parameters described in Section 3.

spectrum. As the filament is only observed in X-rays, we follow previous study to apply low- and high-energy cut-offs at 0.6 and 60 TeV, respectively (R. Bandiera 2008). The observed filament does not strictly follow a truncated cone, making it difficult to constrain the viewing angle. We nonetheless expect the structure to lie mostly in the plane of the sky, given its nearly constant surface brightness.

Figure 7 shows an X-ray image based on the flux tube model. This is generated with $\phi = \pi/3$ and B -fields of 56 and 42 μG at the injection and exit ends, respectively. The model captures the general features of the filament, and its finite length is attributed to the cutoff in the pitch angle distribution.

The B -field required by our model is somewhat higher than the equipartition values reported, but we note that the equipartition assumption may not hold as particles

traverse through the flux tube without much interaction with the field. At the injection end the B -field is compatible with the typical PWN field of the order of a few tens of μG . On the other hand, the exit end field is larger than the typical ISM field. This can be reconciled if the flux tube extends significantly beyond the cut-off point, so that the B -field continues. Alternatively, plasma instability may boost the fields to such (e.g., B. Olmi et al. 2024).

Our calculation assumes 100% of the pulsar spin-down power injected into the flux tube. For a lower injection rate, a slightly higher magnetic field strength is required to match the observed X-ray flux (synchrotron emissivity scales as B^2). This can be relaxed if the injection process is time dependent. Indeed, there is a hint of brightness fluctuation along the filament between the year 2000 and 2006 epochs (M. de Vries et al. 2022),

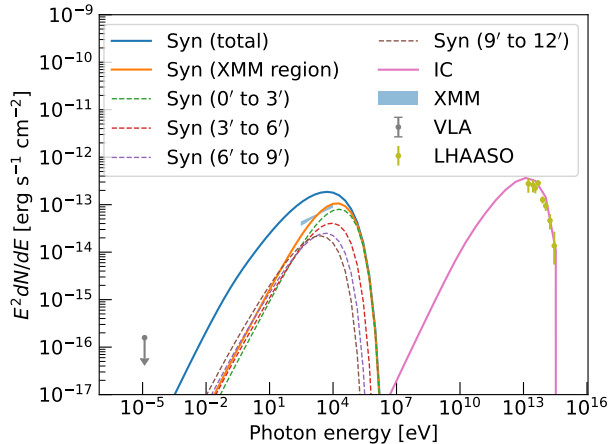


Figure 6. Spectral fit of the two-component model to LHAASO (yellow; *Z. Cao et al. 2025*), XMM-Newton (shaded blue; *W. Benbow et al. 2021*) and VLA (grey upper limit) data. The blue line shows the total synchrotron emission, while the orange line ignores weak extended emission and only considers a region of $1.5' \times 6'$ so it can be compared with the XMM-Newton observation. The corresponding IC emission is shown as the purple line. The dashed lines show the emission in different sections along the flux tube direction, divided into segments of $3'$ length.

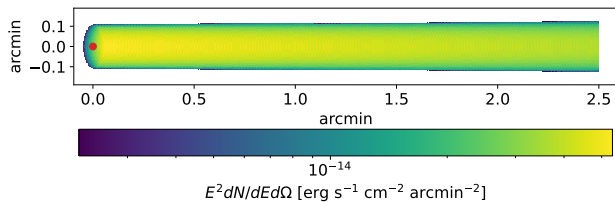


Figure 7. Simulated magnetic flux tube image for the filament of Guitar Nebula at 1 keV. The magnetic fields are assumed to be 56 and $42 \mu\text{G}$ at two ends with a view angle of $\phi = \pi/3$. The projected length and width are chosen to reproduce the measured value.

which could imply a variable injection rate. Finally, we are cautious that the flux tube model has difficulty explaining the short counterfilament observed. The particles there are likely moving away from us, and thus the synchrotron radiation beam would become unobservable, unless there is an additional process, such as scattering, that deflects the particles.

5. CONCLUSION

In this paper, we considered relativistic particles travel along a magnetic flux tube with aligned field structure. The particles in this case would bound to the field lines

without much scattering. We show that in a decreasing field configuration the particles' pitch angles will decrease, resulting in a shrinking emission cone for the synchrotron and IC radiation. This then creates a hard cutoff when the flux tube is viewed off axis. We simulated X-ray and gamma-ray sky images of the flux tube model and found that the synchrotron emission is brightest near the injection end where the B -field is strong. This can create a linear tail-like feature in the X-ray band. On the other hand, the IC gamma rays could show a significant offset from the X-ray tail.

We applied the flux tube model to two PWN cases. First, we show that the X-ray tail of J1740 and the associated TeV emission in the vicinity can be well described by a flux tube plus a diffusion zone. Our model is able to produce the morphology and spectrum of the broadband X-ray to gamma ray emission, and provide constraints on the underlying particle distribution and magnetic field strength. Second, we employed the flux tube model to the misaligned filament of the Guitar Nebula. In our model, the truncation of the filament is naturally explained by the cutoff due to viewing geometry. The B -field we obtained for the Guitar Nebula is slightly higher than the typical PWN value, but this can be reconciled if the flux tube extends beyond the cutoff point.

In a future study, our modeling can be applied to other LHAASO sources associated with bow-shock PWNe and pulsar filaments and, more generally, to any objects with relativistic particles transported by a large-scale aligned magnetic field.

ACKNOWLEDGMENTS

We thank the referee for the constructive advice. This work is supported by the National Natural Science Foundation of China under the grant No. 12375103. This work is supported by a GRF grant of the Hong Kong Government under HKU 17301723. The National Radio Astronomy Observatory and Green Bank Observatory are facilities of the U.S. National Science Foundation operated under cooperative agreement by Associated Universities, Inc. Based on observations obtained with XMM-Newton, an ESA science mission with instruments and contributions directly funded by ESA Member States and NASA.

Facilities: VLA, XMM

Software: CASA (*CASA Team et al. 2022*), naima (*V. Zabalza 2015*), Miriad (*R. J. Sault et al. 1995*)

APPENDIX

A. VLA OBSERVATION OF J1740

The VLA observation of J1740 was performed on 2015 October 23 at the 10 cm band in D configuration. The center frequency is at 3 GHz with a total bandwidth of 2 GHz and the total on-source time is 27 minutes. We processed the data using the CASA package (CASA Team et al. 2022). We first flagged antennas that missed calibrator observations and data affected by severe radio-frequency interference. We then followed the standard procedures to calibrate the flux scale, bandpass, and gains. The Stokes I image is formed using multifrequency synthesis with a beam size of $0.64' \times 0.29'$. The resulting image is shown in Figure 4, which has an rms noise level of $41 \mu\text{Jy beam}^{-1}$. The pulsar is clearly detected with a flux density of $2.8 \pm 0.1 \text{ mJy}$, and the emission is consistent with a point source. The PWN is not detected in the radio image. For its size of $1.5' \times 6'$ as found in the the XMM-Newton observation, we deduce a 3σ flux density limit of 5.3 mJy . This is plotted in Figure 6 and compared with the X-ray spectrum obtained with XMM-Newton. It is obvious that the limit is incompatible with an extrapolation of the simple power-law X-ray spectrum. These can be reconciled if there is a spectral break between the X-ray and radio bands.

REFERENCES

- Abeyssekara, A. U., Albert, A., Alfaro, R., et al. 2017, *Science*, 358, 911, doi: [10.1126/science.aan4880](https://doi.org/10.1126/science.aan4880)
- Aharonian, F. A., Kelner, S. R., & Prosekin, A. Y. 2010, *PhRvD*, 82, 043002, doi: [10.1103/PhysRevD.82.043002](https://doi.org/10.1103/PhysRevD.82.043002)
- Atoyan, A. M., Aharonian, F. A., & Völk, H. J. 1995, *PhRvD*, 52, 3265, doi: [10.1103/PhysRevD.52.3265](https://doi.org/10.1103/PhysRevD.52.3265)
- Bandiera, R. 2008, *A&A*, 490, L3, doi: [10.1051/0004-6361:200810666](https://doi.org/10.1051/0004-6361:200810666)
- Bao, Y., Giacinti, G., Liu, R.-Y., Zhang, H.-M., & Chen, Y. 2025, *PhRvL*, 135, 191002, doi: [10.1103/xqvb-lkrr](https://doi.org/10.1103/xqvb-lkrr)
- Barkov, M. V., Lyutikov, M., & Khangulyan, D. 2019a, *MNRAS*, 484, 4760, doi: [10.1093/mnras/stz213](https://doi.org/10.1093/mnras/stz213)
- Barkov, M. V., Lyutikov, M., Klingler, N., & Bordas, P. 2019b, *MNRAS*, 485, 2041, doi: [10.1093/mnras/stz521](https://doi.org/10.1093/mnras/stz521)
- Beck, M. C., Beck, A. M., Beck, R., et al. 2016, *JCAP*, 2016, 056, doi: [10.1088/1475-7516/2016/05/056](https://doi.org/10.1088/1475-7516/2016/05/056)
- Benbow, W., Brill, A., Buckley, J. H., et al. 2021, *ApJ*, 916, 117, doi: [10.3847/1538-4357/ac05b9](https://doi.org/10.3847/1538-4357/ac05b9)
- Brunelli, G., Ponti, G., Zhang, H., et al. 2025, *A&A*, 704, A30, doi: [10.1051/0004-6361/202554761](https://doi.org/10.1051/0004-6361/202554761)
- Cao, Z., Aharonian, F., Bai, Y. X., et al. 2025, *The Innovation*, 6, 100802, doi: [10.1016/j.xinn.2025.100802](https://doi.org/10.1016/j.xinn.2025.100802)
- CASA Team, Bean, B., Bhatnagar, S., et al. 2022, *PASP*, 134, 114501, doi: [10.1088/1538-3873/ac9642](https://doi.org/10.1088/1538-3873/ac9642)
- de Vries, M., Romani, R. W., Kargaltsev, O., et al. 2022, *ApJ*, 939, 70, doi: [10.3847/1538-4357/ac9794](https://doi.org/10.3847/1538-4357/ac9794)
- Deller, A. T., Goss, W. M., Brisken, W. F., et al. 2019, *ApJ*, 875, 100, doi: [10.3847/1538-4357/ab11c7](https://doi.org/10.3847/1538-4357/ab11c7)
- Dinsmore, J. T., & Romani, R. W. 2024, *ApJ*, 976, 4, doi: [10.3847/1538-4357/ad8344](https://doi.org/10.3847/1538-4357/ad8344)
- Epstein, R. I. 1973, *ApJ*, 183, 593, doi: [10.1086/152250](https://doi.org/10.1086/152250)
- Epstein, R. I., & Petrosian, V. 1973, *ApJ*, 183, 611, doi: [10.1086/152251](https://doi.org/10.1086/152251)
- H. E. S. S. Collaboration, Abramowski, A., Acero, F., et al. 2011, *A&A*, 528, A143, doi: [10.1051/0004-6361/201015381](https://doi.org/10.1051/0004-6361/201015381)
- Jansson, R., & Farrar, G. R. 2012, *ApJ*, 757, 14, doi: [10.1088/0004-637X/757/1/14](https://doi.org/10.1088/0004-637X/757/1/14)
- Kargaltsev, O., Misanovic, Z., Pavlov, G. G., Wong, J. A., & Garmire, G. P. 2008, *ApJ*, 684, 542, doi: [10.1086/589145](https://doi.org/10.1086/589145)
- Kolmogorov, A. 1941, *Akademiia Nauk SSSR Doklady*, 30, 301
- Krumholz, M. R., Crocker, R. M., Bahramian, A., & Bordas, P. 2024, *Nature Astronomy*, 8, 1284, doi: [10.1038/s41550-024-02337-1](https://doi.org/10.1038/s41550-024-02337-1)
- Lai, A. C. M., & Ng, K. C. Y. 2023, *PhRvD*, 107, 063026, doi: [10.1103/PhysRevD.107.063026](https://doi.org/10.1103/PhysRevD.107.063026)
- Lai, P. C. W., Li, K. J., Yap, Y. X. J., Wu, K., & Kong, A. K. H. 2025, *MNRAS*, 542, 902, doi: [10.1093/mnras/staf1295](https://doi.org/10.1093/mnras/staf1295)
- Longair, M. S. 2011, *High Energy Astrophysics*
- Morlino, G., Lyutikov, M., & Vorster, M. 2015, *MNRAS*, 454, 3886, doi: [10.1093/mnras/stv2189](https://doi.org/10.1093/mnras/stv2189)
- Ng, C.-Y., Gaensler, B. M., Chatterjee, S., & Johnston, S. 2010, *ApJ*, 712, 596, doi: [10.1088/0004-637X/712/1/596](https://doi.org/10.1088/0004-637X/712/1/596)
- Olmi, B., Amato, E., Bandiera, R., & Blasi, P. 2024, *A&A*, 684, L1, doi: [10.1051/0004-6361/202449382](https://doi.org/10.1051/0004-6361/202449382)
- Olmi, B., & Bucciantini, N. 2019a, *MNRAS*, 488, 5690, doi: [10.1093/mnras/stz2089](https://doi.org/10.1093/mnras/stz2089)
- Olmi, B., & Bucciantini, N. 2019b, *MNRAS*, 490, 3608, doi: [10.1093/mnras/stz2819](https://doi.org/10.1093/mnras/stz2819)

- Olmi, B., & Bucciantini, N. 2019c, MNRAS, 484, 5755, doi: [10.1093/mnras/stz382](https://doi.org/10.1093/mnras/stz382)
- Qin, G., Zhang, M., & Dwyer, J. R. 2006, Journal of Geophysical Research (Space Physics), 111, A08101, doi: [10.1029/2005JA011512](https://doi.org/10.1029/2005JA011512)
- Recchia, S., Di Mauro, M., Aharonian, F. A., et al. 2021, PhRvD, 104, 123017, doi: [10.1103/PhysRevD.104.123017](https://doi.org/10.1103/PhysRevD.104.123017)
- Rigoselli, M., Mereghetti, S., Anzuinelli, S., et al. 2022, MNRAS, 513, 3113, doi: [10.1093/mnras/stac1130](https://doi.org/10.1093/mnras/stac1130)
- Rybicki, G. B., & Lightman, A. P. 1979, Radiative processes in astrophysics
- Sault, R. J., Teuben, P. J., & Wright, M. C. H. 1995, in Astronomical Society of the Pacific Conference Series, Vol. 77, Astronomical Data Analysis Software and Systems IV, ed. R. A. Shaw, H. E. Payne, & J. J. E. Hayes, 433, doi: [10.48550/arXiv.astro-ph/0612759](https://doi.org/10.48550/arXiv.astro-ph/0612759)
- Yan, K., Wu, S., & Liu, R.-Y. 2025, ApJ, 987, 19, doi: [10.3847/1538-4357/add6a4](https://doi.org/10.3847/1538-4357/add6a4)
- Yang, Y.-P., & Zhang, B. 2018, ApJL, 864, L16, doi: [10.3847/2041-8213/aada4f](https://doi.org/10.3847/2041-8213/aada4f)
- Zabalza, V. 2015, in International Cosmic Ray Conference, Vol. 34, 34th International Cosmic Ray Conference (ICRC2015), 922, doi: [10.22323/1.236.0922](https://doi.org/10.22323/1.236.0922)